Article

Limits on gas impermeability of graphene

P. Z. Sun[1,2], Q. Yang[1,2], W. J. Kuang[1], Y. V. Stebunov[1,2], W. Q. Xiong[3], J. Yu[4], R. R. Nair[2], M. I. Katsnelson[4], S. J. Yuan[3,4 ✉], I. V. Grigorieva[1], M. Lozada-Hidalgo[1], F. C. Wang[1,2,5] & A. K. Geim[1,2 ✉]

Despite being only one-atom thick, defect-free graphene is considered to be completely impermeable to all gases and liquids[1–10]. This conclusion is based on theory[3–8] and supported by experiments[1,9,10] that could not detect gas permeation through micrometre-size membranes within a detection limit of 10^5 to 10^6 atoms per second. Here, using small monocrystalline containers tightly sealed with graphene, we show that defect-free graphene is impermeable with an accuracy of eight to nine orders of magnitude higher than in the previous experiments. We are capable of discerning (but did not observe) permeation of just a few helium atoms per hour, and this detection limit is also valid for all other gases tested (neon, nitrogen, oxygen, argon, krypton and xenon), except for hydrogen. Hydrogen shows noticeable permeation, even though its molecule is larger than helium and should experience a higher energy barrier. This puzzling observation is attributed to a two-stage process that involves dissociation of molecular hydrogen at catalytically active graphene ripples, followed by adsorbed atoms flipping to the other side of the graphene sheet with a relatively low activation energy of about 1.0 electronvolt, a value close to that previously reported for proton transport[11,12]. Our work provides a key reference for the impermeability of two-dimensional materials and is important from a fundamental perspective and for their potential applications.

From a theoretical standpoint, monolayer graphene poses a very high energy barrier for the penetration of atoms and molecules. Density functional theory (DFT) calculations predict that the energy barrier E is at least several electronvolts[2–6], which should prohibit any gas permeation under ambient conditions. Indeed, one can estimate that at room temperature, it would take longer than the lifetime of the Universe to find an atom energetic enough to pierce a defect-free membrane of any realistic size. These expectations agree with experiments that have reported no detectable gas permeation through mechanically exfoliated graphene. The highest sensitivity was achieved using micrometre-size wells etched in oxidized silicon wafers, which were sealed with graphene[1,9,10]. In those measurements, a pressurized gas (for example, helium) could permeate along the SiO_2 layer and gradually fill the microcontainers, making so-called nanoballoons. Their consecutive deflation in air was monitored using atomic force microscopy (AFM) and it was shown that the leakage occurred along only the SiO_2 surface, within minutes but independently of the number of graphene layers used for the sealing[1]. These studies allowed the conclusion that graphene membranes are impermeable to all gases, at least with the achieved accuracy of 10^5–10^6 atoms per second. This was further corroborated by creating individual atomic-scale defects in graphene nanoballoons, which resulted in their relatively fast deflation/inflation and confirmed the exceptionally high sensitivity of the method[9,10].

The devices used in this study were micrometre-size containers made from monocrystals of graphite or hexagonal boron nitride (hBN) using electron-beam lithography and dry etching (Fig. 1, Extended Data Fig. 1). The containers were sealed with graphene monolayer crystals obtained by mechanical exfoliation and transferred on top of the wells using van der Waals assembly ('Device fabrication' in Methods). In control experiments, bilayer graphene and monolayer molybdenum disulfide (MoS_2) were used for the sealing (see further below and in Methods). The wells were chosen to have an inner diameter d of 0.5 or 1.0 µm, and their depth h was about 50 nm to minimize the containers' volume and, therefore, maximize the sensitivity with respect to the number of inflowing gas molecules. The depth could not be reduced further because van der Waals attraction of graphene to the inner walls caused it to sag[1,13,14], typically by a few tens of nanometres (Fig. 1c, d). The wells' ring-shaped top was typically 1-µm wide to provide a sufficiently large atomically flat area so that no gas diffusion could occur along the resulting 'atomically tight' sealing with its clean and atomically sharp interface[15,16]. The monocrystalline walls of our microcontainers were also impermeable, as reported previously[17] and confirmed in the present work using wells with walls of different thicknesses. The rough surface outside the wells (due to etching) helped to pin the membranes, preventing their slippage. The atomically tight sealing is the principal difference with respect to the previous experimental setup[1,9,10] that used 'leaky' SiO_2. In our design, the only possible route for the gas ingress/escape is through the two-dimensional (2D) membrane.

The basic principle used for detection of molecular penetration through graphene membranes is similar to that introduced in ref. [1] and illustrated in Fig. 1a. The described microcontainers were placed inside a chosen gas atmosphere (for example, helium) and, if graphene

[1]Department of Physics and Astronomy, University of Manchester, Manchester, UK. [2]National Graphene Institute, University of Manchester, Manchester, UK. [3]Key Laboratory of Artificial Micro- and Nano-structures of Ministry of Education, School of Physics and Technology, Wuhan University, Wuhan, China. [4]Institute for Molecules and Materials, Radboud University, Nijmegen, The Netherlands. [5]Chinese Academy of Sciences Key Laboratory of Mechanical Behavior and Design of Materials, Department of Modern Mechanics, University of Science and Technology of China, Hefei, China. ✉e-mail: s.yuan@whu.edu.cn; geim@manchester.ac.uk
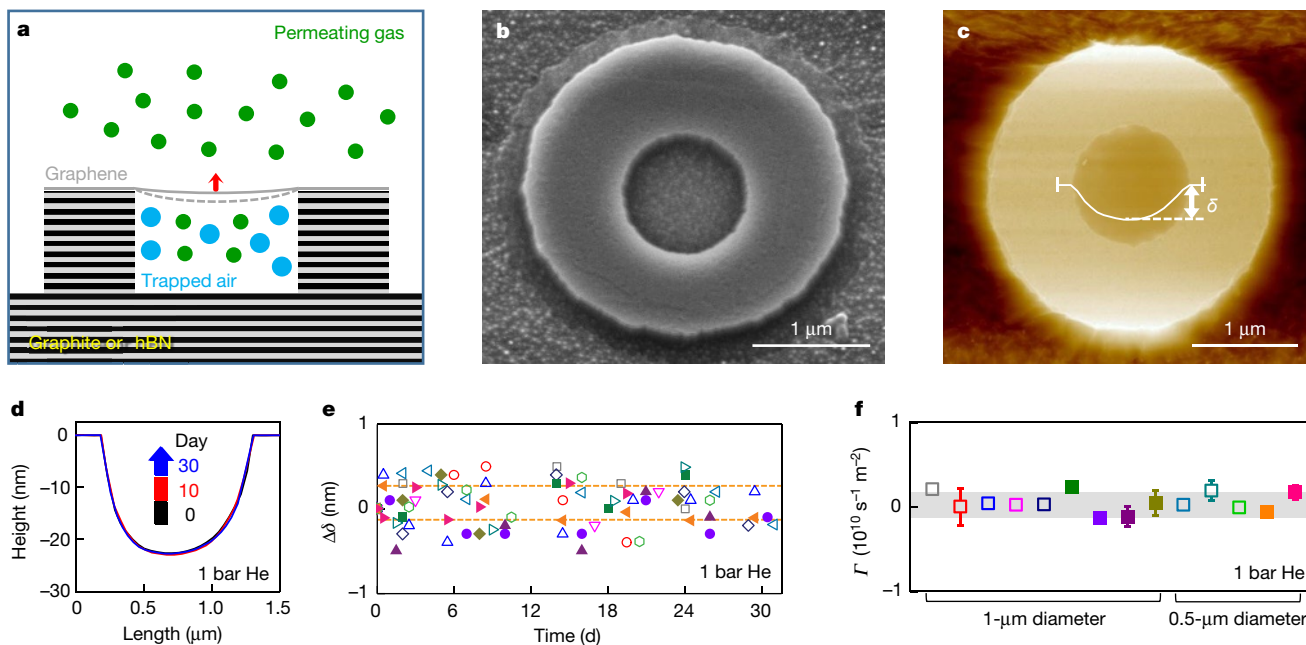
Fig. 1 | The impermeability of graphene to helium. a, Schematic of our experimental setup. **b**, Electron micrograph of one of the studied containers. The image was taken at a tilt angle of 20° for a better view. The graphene membrane is seen to stretch over the outer wall and attach to the dry-etched surface outside. **c**, AFM image of a similar device. The white curve shows the profile of the suspended graphene along the well's diameter. The vertical bars indicate the width (about 150 nm) over which such profiles were averaged. **d**, Examples of AFM profiles for the same container after storing it in helium for days (colour coded). **e**, Changes in the maximum deflection point for 14 containers placed in helium over a one-month period. Different symbols denote containers made from graphite (empty symbols) and hBN (solid). The orange lines indicate the experimental scatter (full range of observed $\Delta\delta$) for one of the devices represented by the same colour. **f**, Permeation rates Γ evaluated from the data in **e**; same symbol coding. Error bars are standard deviation by fitting δ with the linear time dependence. The grey area indicates the overall standard deviation using the data for all the devices.

were permeable to it, the partial pressures inside and outside should equalize so that the total pressure inside the containers (filled with the less permeating air) would increase with time, resulting in gradual lifting and eventual bulging of the membranes. Changes in the membrane position were monitored with AFM. All the containers were first checked for any possible damage to their sealing and the absence of atomic-scale defects[9,10] as described in Methods ('Experimental procedures'). Only the containers that successfully passed the initial tests were investigated further. They were placed in helium, initially for a few days. After that, the devices were taken out, measured by AFM within 10 min to detect minute changes in the membrane position δ (Fig. 1c) and quickly placed back for further exposure to helium. To maximize our accuracy, AFM mapping was carried out using the PeakForce mode and, for repeated measurements, scans were taken in the same direction over the same area ('AFM measurements' in Methods). For the same reason, we minimized the stress imposed by different pressures inside and outside the containers by normally keeping the external pressure P_a at 1 bar and varying only the partial pressure P of the tested gas (Methods). Furthermore, we avoided containers with d larger than 1 µm because their scans appeared notably noisier ('AFM measurements' in Methods). Our experiments were limited to temperatures $T \leq 60\,°C$ because, after thermal cycling to higher T, graphene membranes were often destroyed, probably because of strain induced by thermal expansion/contraction (Extended Data Fig. 2).

Under exposure to helium, no changes in δ could be detected, as detailed in Fig. 1d–f, Extended Data Fig. 3. The figures show that the membrane positions did not change regardless of how long they were exposed to helium. For example, Fig. 1e plots our results for more than a dozen containers over an observation period of one month. None of the devices showed any discernible changes ($\Delta\delta$) in the membranes' original positions, beyond small random fluctuations that did not exceed 0.5 nm in amplitude. Statistical analysis of the $\Delta\delta$ values yielded

a standard deviation of about 1 Å (Fig. 1e; 'AFM measurements' in Methods). In control experiments, we carried out the same measurements in air and found fluctuations of a similar amplitude (Extended Data Fig. 3). For higher applied P, the fluctuations were slightly stronger, presumably because the extra pressure caused creep of the membranes (Extended Data Fig. 3).

For small changes $\Delta\delta$ in the membrane position, the number of atoms or molecules ΔN penetrating through the area S is given by[9,18]

$$\Delta N = c\frac{P_a}{k_B T}S\Delta\delta \qquad (1)$$

where $k_B T$ is the thermal energy, k_B is the Boltzmann constant and $c \approx 0.5$ is the coefficient that accounts for the membrane's curved profile ('Evaluation of permeation rates and their accuracy' in Methods). The above accuracy of roughly 1 Å over one month translates into no more than a few atoms entering the microcontainers per hour. This accuracy is more than eight orders of magnitude higher than that achieved in the earlier experiments reporting graphene's impermeability[1,9,10], which were in turn a few orders of magnitude more sensitive than the detection limit of modern helium leak detectors. In terms of the areal permeation rates $\Gamma = (\mathrm{d}\Delta N/\mathrm{d}t)/S$, our experiments yield an upper bound of about $10^9\,s^{-1}\,m^{-2}$ for possible helium transparency of defect-free graphene. To put this into perspective, monolayer graphene is less permeable than 1-km-thick quartz glass. Furthermore, the found limit allows a lower-bound estimate for the energy barrier E that graphene presents for helium atoms. Using the expression ('Energy barriers' in Methods)

$$\Gamma = \frac{P}{\sqrt{2\pi m k_B T}}\exp\left(-\frac{E}{k_B T}\right) \qquad (2)$$

we obtain $E \geq 1.2$ eV, where the pre-exponential factor describes the incident rate of helium atoms and m is their mass. This estimate is consistent with the barriers found theoretically[2–4]. Keeping in mind that it is hardly possible to improve the accuracy for $\Delta\delta$ beyond 1 Å, the fluctuations increase for larger d, and observations longer than a few months and at considerably higher T are impractical, our results probably present the sensitivity limit of the nanoballoon method.

Helium with its small weakly interacting atoms is recognized as the most permeating of all gases. Nonetheless, we tested several other gases (namely, Ne, N_2, O_2, Ar, Kr and Xe) and, as expected, found no discernible permeation. This places practically the same limit on their E. Unexpectedly, monolayer graphene exhibited noticeable transparency with respect to molecular hydrogen, H_2. We first illustrate this observation qualitatively, by showing in Fig. 2a one of our microcontainers before and after its exposure to hydrogen at 50 °C for 3 d. The membrane clearly bulged up, although the same container passed our impermeability tests with respect to both helium and argon at the same T. This observation is striking because even atomic hydrogen, with a diameter smaller than that of helium, is predicted to experience an E of 2.6–4.6 eV for monolayer graphene[4–6], leaving aside the fact that dissociation of molecular hydrogen requires about 4.5 eV, which makes the concentration of atomic hydrogen negligible. Molecular hydrogen is expected[3] to have even higher E of more than 10 eV. For such high barriers, hydrogen permeation is completely forbidden and, according to equation (2), it should take billions of years for a single hydrogen atom to get inside the container. In another control experiment, we used microcontainers sealed with bilayer graphene and monolayer MoS_2. They exhibited no detectable permeation under multiday exposure to molecular hydrogen at 50 °C (Extended Data Fig. 4).

To quantify the observed hydrogen permeation, we measured changes in δ as a function of time for many devices at room temperature (295 ± 2 K). They exhibited approximately the same inflation rates within scatter of about ±15%, as indicated by the dashed lines in Fig. 2b, which yields $\Gamma \approx 2 \times 10^{10}$ s^{-1} m^{-2}. Note that such a minute gas influx is far beyond the detection limit for microcontainers with SiO_2 sealing[1,9,10]. Furthermore, working in the regime of small linear-in-time $\Delta\delta$ (no bulging as in Fig. 2a), we measured hydrogen permeation at different T. The temperature dependences followed the Arrhenius law, $\Gamma \propto \exp(-E/k_BT)$, yielding an activation barrier of 1.0 ± 0.1 eV (Fig. 2c). This relatively small E strongly disagrees with the theoretical expectations and, more importantly, with the fact that smaller helium atoms did not penetrate through the same membranes.

Trying to understand the origin of the unexpected behaviour, we performed two additional sets of experiments. First, we quantified the hydrogen permeation rates at different pressures P and found $\Gamma \propto P^{1/2}$ (Extended Data Fig. 5). The square-root dependence is characteristic of processes involving an equilibrium between adsorbed and desorbed constituents of a bipartite gas[19], in contrast to the linear dependence of equation (2) valid for weakly interacting atoms ('Energy barriers' in Methods). Second, we measured permeation for hydrogen's isotope deuterium. Within our detection limit, no permeation could be discerned, which puts a limit of $\Gamma \leq 10^9$ s^{-1} m^{-2} on the deuterium influx ('Isotope effect' in Methods and Extended Data Fig. 8).

To understand the reason for the exclusivity of hydrogen among the other gases, let us recall the following facts. Locally curved and strained graphene surfaces are known experimentally to be chemically reactive[20,21] and are expected to lower the energy required for dissociation of molecular hydrogen[22,23]. For a local protrusion (ripple) with $t/D \geq 5\%$ (where t is its height and D the lateral size), the dissociated state with two hydrogen adatoms becomes energetically more favourable[22,23], whereas the energy barrier required to reach this state is also reduced to about 1 eV ('Ab initio simulations of graphene's catalytic activity' in Methods). This catalytic activity of graphene is relevant because suspended membranes exhibit extensive nanoscale rippling[24–26] with t/D that can easily exceed 5% for both static[24,25] and dynamic[26] ripples
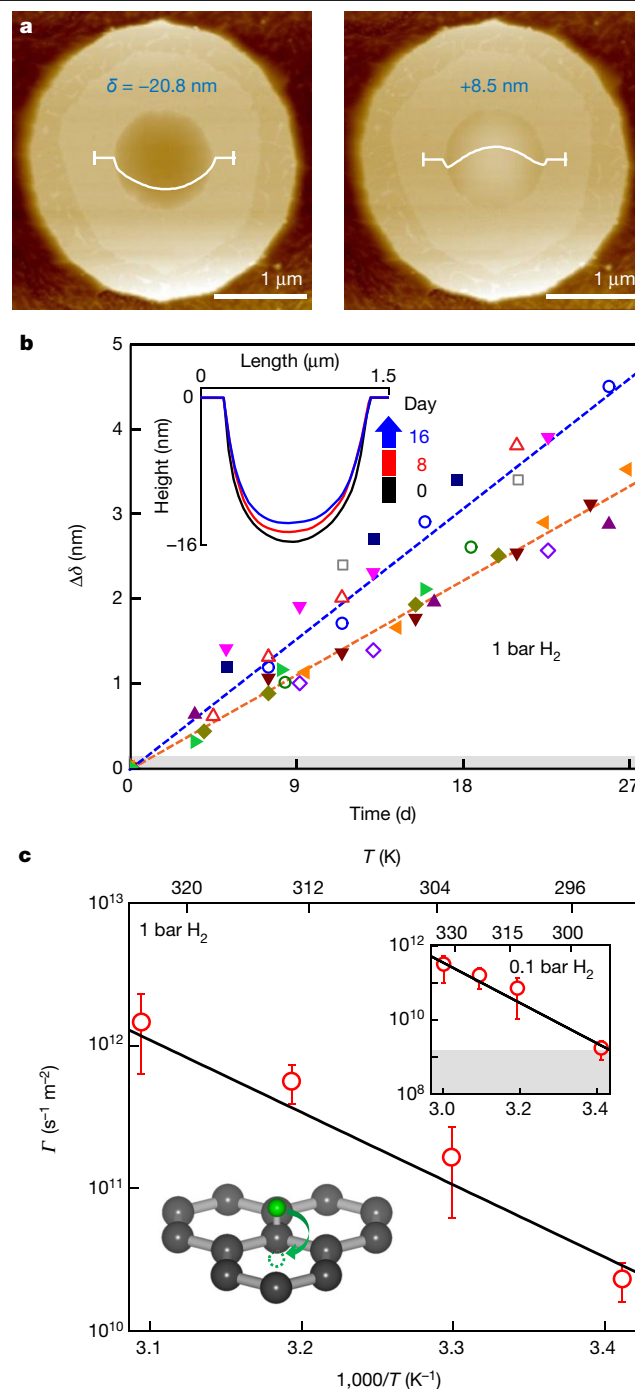

Fig. 2 | Hydrogen permeation through defect-free graphene. a, AFM micrographs of the same microcontainer before (left) and after (right) storing it for 3 d in molecular hydrogen at 1 bar. To speed up permeation, the gas was heated to 50 °C. White curves show the height profiles along the well's diameter. Tens of microcontainers were tested, showing the same effect. The somewhat darker outside region of the well's top appears because it is not atomically flat but slightly tapered (our lithography masks often thinned towards the outside perimeter, allowing some plasma etching of the rim region). **b**, Time evolution of $\Delta\delta$ for 12 different devices in molecular hydrogen at 1 bar at $T = 295 \pm 2$ K. The empty and solid symbols denote graphite and hBN wells, respectively. Blue and orange dashed lines are the best linear fits for two of the devices (colour coded) to indicate experimental scatter. Inset: representative changes in the AFM profiles with time. **c**, Hydrogen permeation rates at different T. Symbols are experimental data and the solid curve is the best fit to the activation behaviour, which yields $E = 1.0 \pm 0.1$ eV. Top inset: same as the main panel, but for $P = 0.1$ bar. Error bars are standard deviation using six or more devices for each T. Bottom inset: illustration of the flipping process in the suggested mechanism of hydrogen permeation. The grey areas in **b**, **c** indicate our detection limit.

Article

Another fact is that monolayer graphene is known to be highly permeable to protons, exhibiting an activation energy of 1.0 ± 0.05 eV, whereas bilayer graphene and monolayer MoS_2 exhibit no detectable proton permeation[11,12]. This is relevant because a hydrogen atom absorbed on graphene shares its electron with the conducting surface and is indistinguishable from an adsorbed proton. Furthermore, it is also known that deuterons, nuclei of deuterium atoms, experience a higher barrier than protons, which drastically slows their permeation through monolayer graphene[12] ('Isotope effect' in Methods).

On the basis of the above facts, we propose the following scenario for the observed hydrogen permeation. First, molecular hydrogen is chemisorbed (adsorbed and dissociated) on graphene ripples, which results in sp^3-bonded adatoms as illustrated in Extended Data Fig. 6. These adatoms then flip to the other side of graphene in a 1.0-eV transfer process similar to that previously reported for proton transport[11,12] (inset of Fig. 2c). The flipped adatoms subsequently desorb from the concave surface. This scenario is fully consistent with all the experimental evidence and, also, explains why the observed permeation is limited to hydrogen and monolayer graphene. Indeed, among the tested 2D crystals, only the latter is sufficiently transparent to protons. Neither bilayer graphene nor monolayer MoS_2 allow protons through[11], whereas monolayer graphene presents a notably higher barrier for heavier deuterons than protons[12] (see 'Isotope effect' in Methods).

Although our experiments cannot distinguish directly whether it is chemisorption or flipping that limits the hydrogen permeation, the close match of the measured E with the value reported in ref. [12] hints that the flipping is likely to be the rate-limiting process. This is also supported by the observed isotope effect. Indeed, our DFT calculations could not find any influence of zero-point oscillations on hydrogen's dissociation (see 'Isotope effect' in Methods). However, the flipping is expected to exhibit an isotope shift because zero-point oscillations decrease the energy of the initial state in the transfer process[12]. This shift results in a higher effective barrier for deuterium and makes its permeation undetectable in our experiments (see 'Isotope effect' in Methods). The dependence $\Gamma \propto P^{1/2}$ (suggesting a finite coverage of graphene with hydrogen) is also consistent with the flipping step being the limiting factor. Indeed, it is easier for lighter adatoms to desorb from graphene (because of stronger zero-point oscillations), which should result in higher coverage of the graphene surface with deuterium. Accordingly, if chemisorption were the limiting step, higher permeation rates would be expected for deuterium rather than hydrogen, contrary to our observations.

To conclude, defect-free graphene should be completely impermeable to all atomic and molecular species at room temperature, but ripples, wrinkles and other defects inducing a local curvature are catalytically active and allow non-negligible permeation of hydrogen. If necessary, the latter can be blocked by using bilayer graphene or other 2D materials such as monolayer MoS_2. Our results have implications for many observations in the literature. For example, ripples are likely to play an important role in lowering barriers for proton transport through 2D membranes[11,12], a distinct possibility not considered so far theoretically[7,27–29]. Similarly, the observations may shed light on the intercalation of graphene on silicon carbide by molecular hydrogen that is argued to permeate through defect-free graphene[30,31]. The discussed processes may also be critical for the interaction of graphene with water and hydrocarbons and, more generally, emphasize unexpectedly high catalytic activity of non-flat graphene, in stark contrast to the extreme chemical inertness of its bulk counterpart, graphite.

Online content

Any methods, additional references, Nature Research reporting summaries, source data, extended data, supplementary information, acknowledgements, peer review information; details of author contributions and competing interests; and statements of data and code availability are available at https://doi.org/10.1038/s41586-020-2070-x.

1. Bunch, J. S. et al. Impermeable atomic membranes from graphene sheets. *Nano Lett.* **8**, 2458–2462 (2008).
2. Berry, V. Impermeability of graphene and its applications. *Carbon* **62**, 1–10 (2013).
3. Leenaerts, O., Partoens, B. & Peeters, F. M. Graphene: a perfect nanoballoon. *Appl. Phys. Lett.* **93**, 193107 (2008).
4. Tsetseris, L. & Pantelides, S. T. Graphene: an impermeable or selectively permeable membrane for atomic species? *Carbon* **67**, 58–63 (2014).
5. Miao, M., Nardelli, M. B., Wang, Q. & Liu, Y. First principles study of the permeability of graphene to hydrogen atoms. *Phys. Chem. Chem. Phys.* **15**, 16132–16137 (2013).
6. Seel, M. & Pandey, R. Proton and hydrogen transport through two-dimensional monolayers. *2D Mater.* **3**, 025004 (2016).
7. Feng, Y. et al. Hydrogenation facilitates proton transfer through two-dimensional honeycomb crystals. *J. Phys. Chem. Lett.* **8**, 6009–6014 (2017).
8. Wang, W. L. & Kaxiras, E. Graphene hydrate: theoretical prediction of a new insulating form of graphene. *New J. Phys.* **12**, 125012 (2010).
9. Koenig, S. P., Wang, L., Pellegrino, J. & Bunch, J. S. Selective molecular sieving through porous graphene. *Nat. Nanotechnol.* **7**, 728–732 (2012).
10. Wang, L. et al. Molecular valves for controlling gas phase transport made from discrete ångström-sized pores in graphene. *Nat. Nanotechnol.* **10**, 785–790 (2015).
11. Hu, S. et al. Proton transport through one-atom-thick crystals. *Nature* **516**, 227–230 (2014).
12. Lozada-Hidalgo, M. et al. Sieving hydrogen isotopes through two-dimensional crystals. *Science* **351**, 68–70 (2016).
13. Bunch, J. S. et al. Electromechanical resonators from graphene sheets. *Science* **315**, 490–493 (2007).
14. Radha, B. et al. Molecular transport through capillaries made with atomic-scale precision. *Nature* **538**, 222–225 (2016).
15. Haigh, S. J. et al. Cross-sectional imaging of individual layers and buried interfaces of graphene-based heterostructures and superlattices. *Nat. Mater.* **11**, 764–767 (2012).
16. Kelly, D. J. et al. Nanometer resolution elemental mapping in graphene-based TEM liquid cells. *Nano Lett.* **18**, 1168–1174 (2018).
17. Hu, S. et al. Transport of hydrogen isotopes through interlayer spacing in van der Waals crystals. *Nat. Nanotechnol.* **13**, 468–472 (2018).
18. Koenig, S. P., Boddeti, N. G., Dunn, M. L. & Bunch, J. S. Ultrastrong adhesion of graphene membranes. *Nat. Nanotechnol.* **6**, 543–546 (2011).
19. Deveau, N. D., Ma, Y. H. & Datta, R. Beyond Sieverts' law: a comprehensive microkinetic model of hydrogen permeation in dense metal membranes. *J. Membr. Sci.* **437**, 298–311 (2013).
20. Wu, Q. et al. Selective surface functionalization at regions of high local curvature in graphene. *Chem. Commun.* **49**, 677–679 (2013).
21. Bissett, M. A., Konabe, S., Okada, S., Tsuji, M. & Ago, H. Enhanced chemical reactivity of graphene induced by mechanical strain. *ACS Nano* **7**, 10335–10343 (2013).
22. Boukhvalov, D. W. & Katsnelson, M. I. Enhancement of chemical activity in corrugated graphene. *J. Phys. Chem. C* **113**, 14176–14178 (2009).
23. McKay, H., Wales, D. J., Jenkins, S. J., Verges, J. A. & de Andres, P. L. Hydrogen on graphene under stress: molecular dissociation and gap opening. *Phys. Rev. B* **81**, 075425 (2010).
24. Meyer, J. C. et al. On the roughness of single- and bi-layer graphene membranes. *Solid State Commun.* **143**, 101–109 (2007).
25. Geringer, V. et al. Intrinsic and extrinsic corrugation of monolayer graphene deposited on SiO_2. *Phys. Rev. Lett.* **102**, 076102 (2009).
26. Fasolino, A., Los, J. H. & Katsnelson, M. I. Intrinsic ripples in graphene. *Nat. Mater.* **6**, 858–861 (2007).
27. Kroes, J. M. H., Fasolino, A. & Katsnelson, M. I. Density functional based simulations of proton permeation of graphene and hexagonal boron nitride. *Phys. Chem. Chem. Phys.* **19**, 5813–5817 (2017).
28. Poltavsky, I., Zheng, L., Mortazavi, M. & Tkatchenko, A. Quantum tunneling of thermal protons through pristine graphene. *J. Chem. Phys.* **148**, 204707 (2018).
29. Mazzuca, J. W. & Haut, N. K. Theoretical description of quantum mechanical permeation of graphene membranes by charged hydrogen isotopes. *J. Chem. Phys.* **148**, 224301 (2018).
30. Riedl, C., Coletti, C., Iwasaki, T., Zakharov, A. A. & Starke, U. Quasi-free-standing epitaxial graphene on SiC obtained by hydrogen intercalation. *Phys. Rev. Lett.* **103**, 246804 (2009).
31. Kunc, J., Rejhon, M. & Hlídek, P. Hydrogen intercalation of epitaxial graphene and buffer layer probed by mid-infrared absorption and Raman spectroscopy. *AIP Adv.* **8**, 045015 (2018).

Methods

Device fabrication

Our devices were fabricated as shown schematically in Extended Data Fig. 1a. A monocrystal of either graphite (NGS Naturgraphit) or hBN (HQ Graphene) with a thickness of at least 150 nm was first mechanically exfoliated onto an oxidized silicon wafer that was freshly cleaned in an oxygen plasma. The quality of the crystal's top surface was carefully checked for the presence of atomic terraces using dark-field and differential-interference-contrast microscopy. These modes allow detection of crystal edges, terraces and tears, even for a monolayer thickness. Using e-beam lithography, a set of ring-shaped polymer masks with an inner diameter d of 0.5 or 1.0 μm was patterned on atomically flat parts of the surface (without terraces). Reactive-ion etching was then used to remove roughly 50 nm of the exposed area to form micrometre-diameter wells (Extended Data Fig. 1b). After the lithography mask was dissolved, we annealed the structures in a hydrogen and argon (1:10) atmosphere at 400 °C for 6 h. Then a relatively large crystal of monolayer graphene (also obtained by mechanical exfoliation) was transferred in air on top of the wells using the standard transfer procedures for assembly of van der Waals heterostructures[32,33]. Extended Data Fig. 1b shows an optical image of an array of graphene-sealed hBN wells. Closer views of such microcontainers are provided in Fig. 1, Extended Data Fig. 2a, where one can clearly see graphene membranes draping over the wells. For comparison, Extended Data Fig. 2b shows a broken graphene membrane after our unsuccessful attempt to test it at 80 °C. As the inner walls of the containers are not perfectly round (see, for example, Fig. 1b, c), graphene membranes sag inside in a slightly asymmetric manner as noticeable in some AFM profiles (for example, Fig. 1d).

Experimental procedures

After the fabrication, microcontainers were first checked with AFM for possible tears, wrinkles and other defects. Only devices with seemingly perfect sealing were used for further investigation. Those were tested further by placing them in a 3-bar argon atmosphere overnight. Occasionally, we found inflated containers that deflated quickly in air. In principle, this could be due to defects[9,10,34], but in most cases we could trace the leakage to poor sealing of the microcontainers: either the top surface of the wells was slightly damaged by dry etching so that the rough streaks connected the inner and outer rim edges or small wrinkles were present, as retrospectively revealed by dedicated AFM analysis and scanning electron microscopy. The devices that passed the above tests were placed in a tested gas atmosphere and their possible inflation was carefully monitored as described in the main text.

For gas tests, microcontainers were placed inside a small stainless-steel chamber. It was evacuated to approximately 10^{-3} mbar and then one of the gases under investigation was introduced inside. For studies of temperature dependences, the whole vacuum chamber was placed inside an oven with controllable T.

AFM measurements

To monitor changes in the position of the graphene membranes, we employed the PeakForce mapping mode (Dimension FastScan from Bruker). The use of this AFM mode was essential to achieve the highest possible accuracy in our measurements of the membrane position. The PeakForce mode minimizes tip-to-sample interactions by employing an imaging force that can be as small as about 1 nN and has little effect on suspended graphene. For comparison, when we tried the contact-mode AFM imaging, graphene membranes were found to sag down after each scan by as much as several nanometres, which was obviously unacceptable for our purposes. The PeakForce mode also allows straightforward analysis of the obtained scans, compared with the tapping AFM mode where a non-negligible pressure induced by the tip requires rather involved deconvolution of AFM images[1,35]. Furthermore, to maximize reproducibility between consecutive PeakForce scans, they were taken always along the same direction, x, across the centre of suspended graphene membranes and averaged over a finite width of roughly 150 nm (vertical bars in the shown AFM images). This approach also allowed us to increase accuracy by avoiding changes in AFM profiles caused by the slight asymmetry in membranes' sagging, as pointed out in the Methods section 'Device fabrication'. The asymmetry remains constant during measurements for a given device and does not affect our results. The averaged deflection profile $\delta(x)$ allowed us to detect minor changes $\Delta\delta$ in a membrane's lowest position at the well's centre (denoted above as δ) such that $\delta = \delta(0) + \Delta\delta$, where $\delta(0)$ is the initial-in-time position at the well's centre.

Extended Data Fig. 3a, b shows the accuracy and reproducibility of our measurements of $\delta(x)$ and $\Delta\delta$. For this dataset, two microcontainers were measured in air as described above, and ten AFM scans were taken at 1-h intervals. Between each scan, the devices were taken out of the AFM setup and then placed back to mimic the real measurement procedures. The figures show that the profiles $\delta(x)$ were very stable, and the resulting $\Delta\delta$ did not exceed about 0.3 nm. The statistical uncertainty (standard deviation) for this set of AFM measurements was about 0.16 nm. To check for longer-term stability, 12 microcontainers with $d = 0.5$ and 1.0 μm and different sagging (maximum depth $\delta(0)$ varied between 5 and 25 nm) were kept in air for more than 20 d. Their height profiles were captured at regular intervals, a few days apart. The devices also exhibited excellent stability such that $\Delta\delta$ did not exceed 0.3 nm (Extended Data Fig. 3c), in good agreement with the short-term results in Extended Data Fig. 3a.

After exposing microcontainers to higher helium pressures, we again did not observe any discernible changes in $\delta(x)$ but random fluctuations in $\Delta\delta$ increased (Extended Data Fig. 3e, f), presumably because of additional stresses induced by pressure. Note that, trying to improve our measurement accuracy further, we also made and tested microcontainers with $d \geq 2$ μm. However, their stability was much worse, with $\Delta\delta$ exceeding 1 nm, probably due to increasing instabilities caused by tip–membrane interactions. Data from such wells were not used in the reported analysis.

Evaluation of permeation rates and their accuracy

Equation (1) can be deduced from the expression derived in ref. [9] as follows. The pressure P inside the container includes two components: one is the initial atmospheric pressure of the trapped air (P_a) and the other is ΔP, the pressure change induced by molecular permeation. For small changes in the membrane position, ΔP can be estimated from the Hencky solution[36] as

$$\Delta P = K(\nu)EL(\Delta\delta)^3/a^4 \tag{3}$$

where E is Young's modulus, L is the membrane thickness, a is the radius of the container and $K(\nu)$ is the coefficient that depends on Poisson's ratio ν. For graphene[18,37], $E = 1$ TPa, $\nu = 0.16$ and $K(\nu) = 3.09$. The gas volume inside the container is given by $V = V_0 + \Delta V = Sh + cS\delta$, where S and h are the container's area and depth, respectively, and $c \approx 0.5$ is the numerical coefficient accounting for the curved shape of the membrane. Putting the above expressions for P and V into the ideal gas law $PV = (N_0 + \Delta N)k_BT$ (N_0 is the initial number of air molecules), we find

$$\Delta N = (P_a\Delta V + V_0\Delta P + \Delta P\Delta V)/k_BT \tag{4}$$

Substituting the expressions for ΔV and ΔP, equation (4) can be written as[9]

$$\Delta N = \frac{S}{k_BT}\left[cP_a\Delta\delta + (h + c\delta(0))\frac{K(\nu)EL}{a^4}(\Delta\delta)^3 + c\frac{K(\nu)EL}{a^4}(\Delta\delta)^4\right] \tag{5}$$

For the known constants and noticing that the largest deflection $\Delta\delta$ used in our quantitative analysis was only about 4 nm, we find that the

Article

second and third terms of equation (5) should not exceed 20% of the linear term's value. Therefore, for the purpose of our analysis, equation (5) can be simplified to equation (1). This also agrees with the fact that $\Delta\delta$ evolved linearly in time, within our experimental scatter (Fig. 2b). If contributions of the nonlinear terms were considerable, $\Delta\delta$ should start evolving nonlinearly as a function of ΔN and, hence, time.

Energy barriers

Helium permeation through the barrier presented by a graphene membrane can be estimated using

$$\Gamma = A\exp\left(-\frac{E}{k_B T}\right) \tag{6}$$

where E is the energy barrier for incident atoms and A is their attempt rate (that is, the number of atoms striking a unit area per second). Weakly interacting helium atoms are not adsorbed onto graphene and, therefore, the attempt rate is given by[38]

$$A = \frac{1}{4}\frac{N}{V}\upsilon_G = \frac{P}{4}\frac{1}{k_B T}\upsilon_G \tag{7}$$

where $\upsilon_G = \sqrt{8k_B T/\pi m}$ is the mean speed of helium atoms and m is their atomic weight. Combining equations (6) and (7), we obtain equation (2). However, if gas atoms or molecules become adsorbed on a graphene surface, like in the case of hydrogen, equation (7) is no longer applicable, and the attempt rate depends on an equilibrium density of adsorbed species. Under the latter circumstances, the different dependence $A \propto \sqrt{P}$ is expected[19], in agreement with our results for hydrogen in Extended Data Fig. 5.

Ab initio simulations of graphene's catalytic activity

Energy barriers for the dissociation of molecular hydrogen on flat and rippled graphene were calculated from first principles using DFT, as implemented in the Vienna ab initio package[39]. The generalized gradient approximation[40] and projected augmented wave were adopted to describe the exchange correlation potential and ion–electron interactions. The kinetic energy cutoff and k-point mesh were set to 500 eV and $7 \times 7 \times 1$, respectively[41]. A vacuum region of 20 Å was used to avoid the periodic interaction. The stress force and energy convergence criteria were chosen as 0.01 eV Å^{-1} and 10^{-5} eV, respectively. The van der Waals interactions were included in the dissociation process and treated by the semi-empirical DFT-D3 method[42,43]. A supercell of 8×8 graphene unit cells was adopted for the simulations, and ripples were characterized by the ratio t/D of their height t to the corrugation diameter D (inset in Extended Data Fig. 6a). The energy barrier for the reaction pathway was calculated using the climbing-image nudged elastic band method, in which the total energies of initial, final and several intermediate states during the reaction process were calculated explicitly[44]. The initial state was constructed as follows[22]. First, we created a corrugated graphene supercell with a certain t/D by allowing the atomic structure to relax under biaxial compression. Next, two hydrogen atoms were attached to specified carbon atoms, and the whole system was allowed to relax to its ground state, during which the positions of unoccupied carbon atoms were fixed to keep the t/D value constant. The relaxed carbon structure was then used as the initial configuration and the electron distribution was optimized during the reaction process.

For a given t/D, there are many possible corrugated configurations. If we consider high-symmetry configurations, the corrugation centre is located either at the top of a carbon atom or between two nearest neighbours or at the hexagon centre. To minimize the dissociation energy, we relaxed the above three structures of rippled graphene with two adsorbed hydrogen atoms and used them as the initial states before hydrogenation. The initialized graphene ripple could be allowed to relax further before chemical reaction, but we found that this caused little effect on the energy barrier. After trying many different configurations and reaction processes, we found that the dissociation energy reached a minimum when two opposed sites in a hexagon were hydrogenated (see the insets in Extended Data Fig. 6a). In Extended Data Fig. 6a, we show changes in the total energy during the reaction process for $t/D = 7.5\%$. The dissociation energy barrier is about 1.1 eV and given by the difference between the initial and highest energy states along the reaction pathway. For comparison, the dissociation energy of molecular hydrogen in vacuum is about 4.5 eV (ref. [45]), which shows that ripples are highly catalytically active.

The dissociation energy depends on where in the unit cell hydrogen atoms are adsorbed. For example, Extended Data Fig. 6b shows the adsorption process for the same t/D as in Extended Data Fig. 6a but with hydrogen atoms attached to the nearest carbon atoms. In this case, the dissociation energy barrier is higher (approximately 2.9 eV). Our results for different ripple curvatures t/D are plotted in Extended Data Fig. 6c. Clearly, the dissociation energy decreases monotonically with increasing curvature, and the changes become rather gradual for $t/D > 4\%$. Note that the critical curvature, at which ripples become energetically favourable for dissociation of molecular hydrogen ($t/D \approx 2.5\%$), is smaller than $t/D \approx 4\%$, which was reported in the earlier study[22]. This is because of improvements in the simulation method and optimized atomistic configurations.

Although graphene membranes are known to contain numerous extrinsic (static) ripples[24,25] that have typical $t/D \approx 5\%$, it is instructive to find what kind of intrinsic (dynamic) ripples one can expect due to thermal fluctuations[26]. To this end, we performed molecular dynamics simulations using the Large-scale Atomic/Molecular Massively Parallel Simulator (LAMMPS)[46] and graphene membranes consisting of 387,200 atoms. Periodic boundary conditions were usually employed to mimic an infinite membrane, but we also performed simulations for finite-size membranes (from about 35 to 100 nm in diameter). The lateral size of ripples (D) ranged between a few and 10 nm, independently of the membrane size. Their typical configurations at different T were obtained after thermalization in 100,000 steps (0.00025 femtoseconds per step) and averaging over 20 of such snapshots (Extended Data Fig. 7a). Extended Data Fig. 7b, c shows the areal density for ripples with $t/D \geq 4\%$, which are most catalytically active. One can see that thermal fluctuations generate many such ripples that can result in dissociation of molecular hydrogen.

It is not clear whether static or dynamic ripples dominate the adsorption–dissociation process for graphene membranes. One of the issues limiting a contribution from thermally excited ripples could be their relatively short lifetimes. Our simulations show that the mean half-life of a ripple, during which its t/D drops to half, is of the order of femtoseconds. For comparison, permeation of adsorbed hydrogen atoms through graphene involves the timescale τ, which can be estimated from their adsorption energy as $E_{ad} = h/\tau$ where h is Planck's constant. For atomic hydrogen on graphene[47,48], E_{ad} is expected to be approximately 0.4–1.0 eV, and this yields τ of a few femtoseconds. This is of the same order of magnitude as the characteristic lifetime of ripples.

Besides static and dynamic ripples, there are strained areas around the rim of our microcontainers, which in principle could also contribute to the observed hydrogen permeation. However, this scenario is ruled out by the experimental fact that the observed permeability was proportional to the membrane's area rather than its circumference. Furthermore, permeation rates were the same for devices with different sagging (varying from about 5 to 40 nm), which led to different strain. The above conclusion is also supported by our DFT calculations in which the chemisorption process was considered for flat graphene under strain. Extended Data Fig. 6d shows that the dissociation energy remains high (about 3 eV) even for strains as high as about 15%. This proves that it is the curvature rather than strain that is important for the chemisorption process.

Isotope effect

The proposed mechanism of hydrogen permeation involves several steps: dissociation of molecular hydrogen on graphene ripples leading to a finite coverage of the surface with hydrogen atoms; flipping of the atoms across the membrane in a proton-like transfer process; and their recombination and desorption as molecular hydrogen. Only the chemisorption and flipping are expected to involve sufficiently high energy barriers as discussed in the main text. To determine which of these two key barriers limits the observed permeation, we performed experiments using deuterium. To this end, ten microcontainers were sealed with monolayer graphene and exposed to deuterium at 1 bar at room temperature. $\Delta\delta$ was monitored as a function of time. In stark contrast to our molecular hydrogen experiments, the devices did not show any discernible changes in $\Delta\delta$ (Extended Data Fig. 8). The absence of deuterium permeation was further verified in elevated-T tests such as those in Fig. 2a. Several devices were exposed to deuterium at 50 °C for 3 d, but none exhibited any bulging, in contrast to the molecular hydrogen experiments of Fig. 2a.

To understand the isotope effect, we carried out DFT calculations for chemisorption of deuterium on rippled graphene. After including corrections due to zero-point oscillations, we found little difference in the dissociation energies with respect to molecular hydrogen (Extended Data Fig. 6). However, desorption of deuterium from the graphene surface should be slower because of the same quantum corrections. Hence, surface coverage for deuterium atoms should be higher than that for hydrogen. The latter isotope effect is well known for both graphene and graphite[47,48] and implies that, if chemisorption were the rate-limiting process, higher permeation rates would have been expected for deuterium rather than molecular hydrogen, contrary to our observations. The latter conclusion indicates again that the limiting process is the proton flipping. Indeed, in this case, one expects another isotope effect analogous to that observed in the transport experiments of refs. [12,49] where deuterons exhibited ten times lower conductivity through graphene than protons. The reduction factor R has been attributed to the fact that deuterons have a lower energy in their initial bound state in Nafion[12,49], which results in an effectively higher barrier for flipping (by $\Delta E \approx 60$ meV). This energy shift leads to the ratio between hydrogen and deuterium permeation, which is given by $R = \exp(\Delta E/k_B T) \approx 10$ (ref. [12]). For the case of atomic hydrogen/deuterium adsorbed on graphite, ΔE was found[48] to be around 90 meV. Assuming the same value for graphene, this shift should result in about 35 times slower permeation of deuterons with respect to protons. Because of the detection limit of about 10^9 s^{-1} m^{-2}, we can only conclude from our experiments that $R \geq 20$, in good agreement with the above expectations. This supports the proposed scenario in which the flipping step limits hydrogen permeation through monolayer graphene.

Data availability

All the mentioned data to support this study and its conclusions are available upon request from P.Z.S. (pengzhan.sun@manchester.ac.uk).

32. Geim, A. K. & Grigorieva, I. V. Van der Waals heterostructures. *Nature* **499**, 419–425 (2013).
33. Wang, L. et al. One-dimensional electrical contact to a two-dimensional material. *Science* **342**, 614–617 (2013).
34. Park, H. G. & Jung, Y. Carbon nanofluidics of rapid water transport for energy applications. *Chem. Soc. Rev.* **43**, 565–576 (2014).
35. Whittaker, J. D., Minot, E. D., Tanenbaum, D. M., McEuen, P. L. & Davis, R. C. Measurement of the adhesion force between carbon nanotubes and a silicon dioxide substrate. *Nano Lett.* **6**, 953–957 (2006).
36. Hencky, H. Uber den spannungzustand in kreisrunden platten mit verschwindender biegungssteiflgeit. *Z. Math. Phys.* **63**, 311–317 (1915).
37. Wang, G. et al. Measuring interlayer shear stress in bilayer graphene. *Phys. Rev. Lett.* **119**, 036101 (2017).
38. Landau, L. D. & Lifshitz, E. M. *Course of Theoretical Physics* Vol. 5 *Statistical Physics* 3rd edn (Pergamon Press, 1980).
39. Kresse, G. & Furthmuller, J. Efficient iterative schemes for ab initio total-energy calculations using a plane-wave basis set. *Phys. Rev. B* **54**, 11169–11186 (1996).
40. Perdew, J. P., Burke, K. & Ernzerhof, M. M. Generalized gradient approximation made simple. *Phys. Rev. Lett.* **77**, 3865–3868 (1996).
41. Monkhorst, H. J. & Pack, J. D. Special points for Brillouin-zone integrations. *Phys. Rev. B* **13**, 5188–5192 (1976).
42. Grimme, S. Semiempirical GGA-type density functional constructed with a long-range dispersion correction. *J. Comput. Chem.* **27**, 1787–1799 (2006).
43. Kerber, T., Sierka, M. & Sauer, J. Application of semiempirical long-range dispersion corrections to periodic systems in density functional theory. *J. Comput. Chem.* **29**, 2088–2097 (2008).
44. Sheppard, D., Xiao, P., Chemelewski, W., Johnson, D. D. & Henkelman, G. A generalized solid-state nudged elastic band method. *J. Chem. Phys.* **136**, 074103 (2012).
45. Herzberg, G. & Monfils, A. The dissociation energies of the H$_2$, HD, and D$_2$ molecules. *J. Mol. Spectrosc.* **5**, 482–498 (1961).
46. Plimpton, S. Fast parallel algorithms for short-range molecular dynamics. *J. Comput. Phys.* **117**, 1–19 (1995).
47. Hornekær, L. et al. Clustering of chemisorbed H(D) atoms on the graphite (0001) surface due to preferential sticking. *Phys. Rev. Lett.* **97**, 186102 (2006).
48. Paris, A. et al. Kinetic isotope effect in the hydrogenation and deuteration of graphene. *Adv. Funct. Mater.* **23**, 1628–1635 (2013).
49. Bukola, S. & Creager, S. E. A charge-transfer resistance model and Arrhenius activation analysis for hydrogen ion transmission across single-layer graphene. *Electrochim. Acta* **296**, 1–7 (2019).

a

Graphite or hBN monocrystal

E-beam lithography and reactive-ion etching

Sealing with monolayer graphene

b

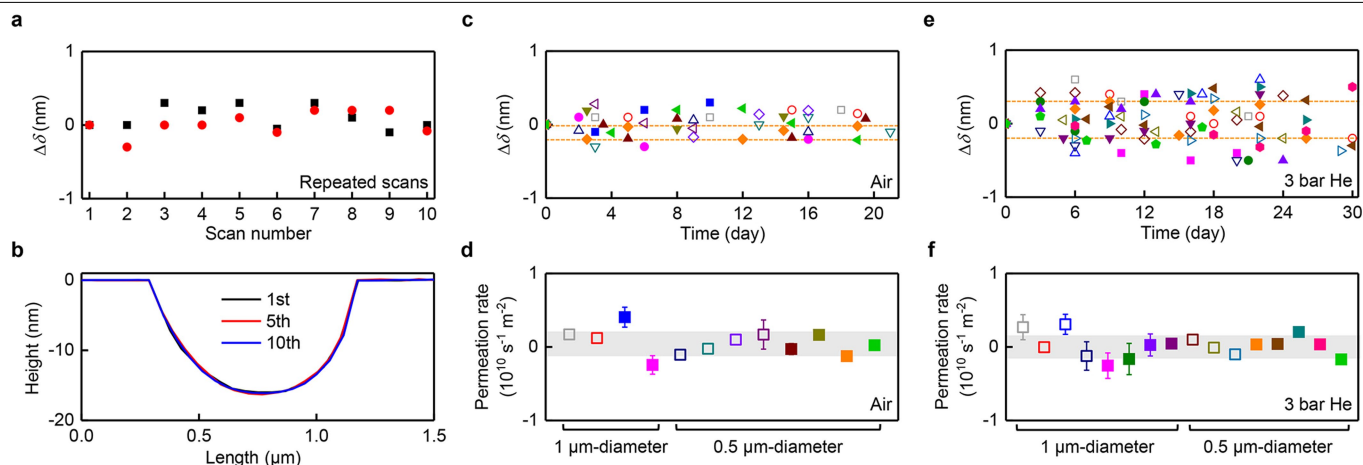Microcontainer

hBN

Graphene

Oxidized silicon wafer

20 μm

Extended Data Fig. 1 | Device fabrication. a, Graphite or hBN monocrystals are obtained by mechanical exfoliation. Micrometre-size wells are then made by e-beam lithography and ion etching. Monolayer graphene is transferred on top to seal the wells. **b**, Optical micrograph of a set of hBN microcontainers. The dashed curve indicates the position of monolayer graphene.
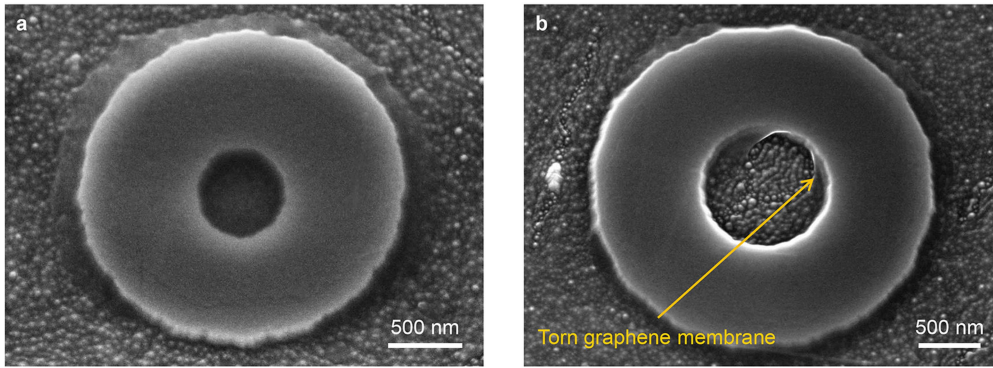
Extended Data Fig. 2 | Electron micrographs of our microcontainers. a, A microcontainer with $d = 0.5\,\mu m$. Such images were taken only after finishing measurements to avoid electron-beam damage. **b**, Example of a broken graphene seal: the membrane was damaged after a thermal cycle to 80 °C.

**Extended Data Fig. 3 | Stability of graphene membranes in air and helium.**
a, Changes in $\delta(0)$ measured for two containers with $d = 1\,\mu m$; AFM scans were taken every hour. **b**, Representative profiles $\delta(x)$ for **a**. **c**, Long-term variations in δ for 12 different containers kept in air. **d**, Permeation rates evaluated from the evolution of $\Delta\delta$ with time in **c**. **e**, $\Delta\delta$ for 16 different devices placed in helium at 3 bar. **f**, Permeation rates for the data in **e**. In **c**, **e**, different symbols denote different microcontainers made from graphite (empty symbols) and hBN (solid). The dashed lines in **c**, **e** indicate maximum changes detected for representative devices (colour coded). In **d**, **f**, the colour represents the same-colour device as in **c**, **e**, respectively. Error bars are standard deviation for fitting δ with a linear time dependence. Grey areas are the overall statistical accuracy obtained using all our devices measured in air and helium at 3 bar.
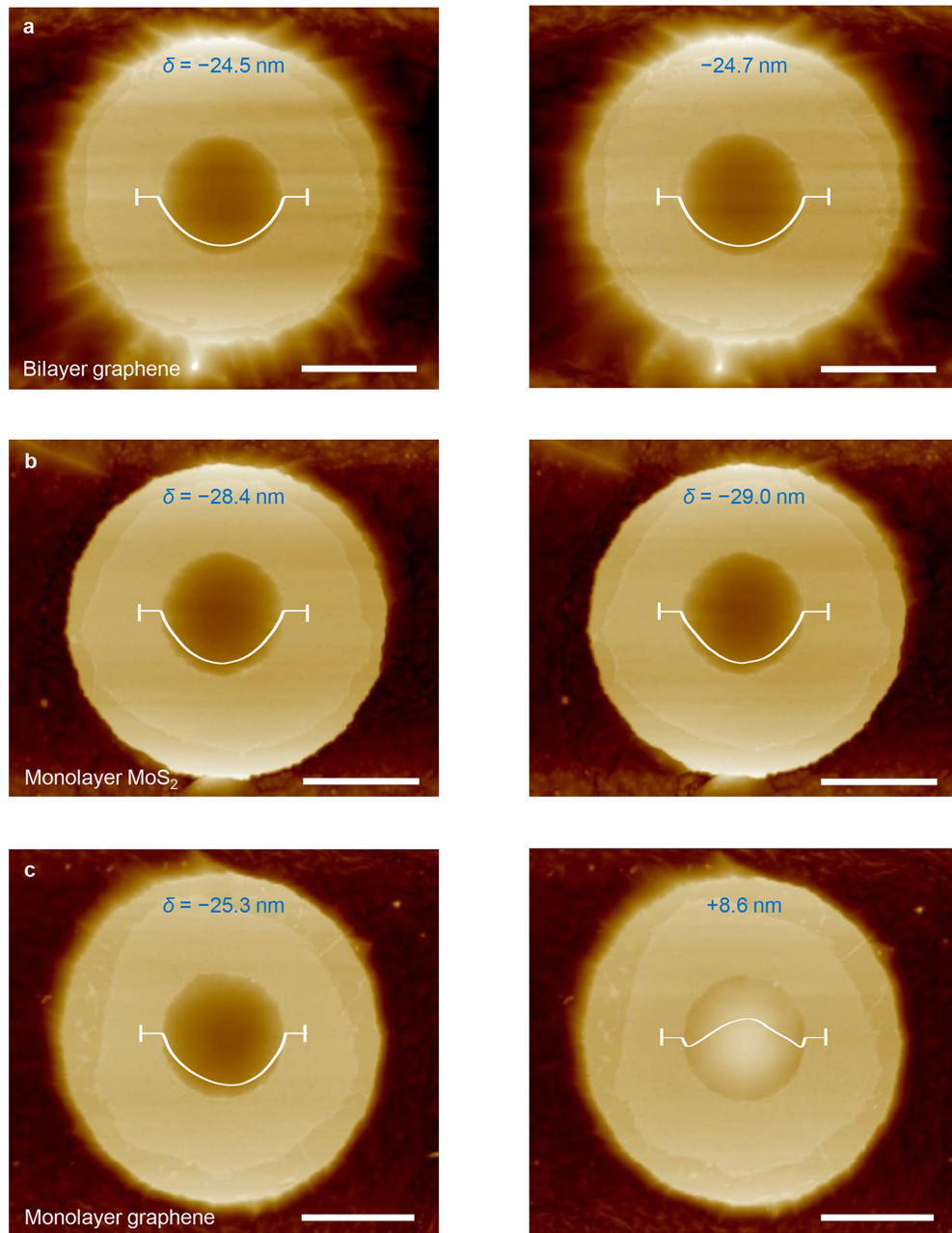
Extended Data Fig. 4 | Bilayer graphene and monolayer MoS$_2$ are impermeable to hydrogen. a, AFM micrographs of the same container sealed with bilayer graphene before (left) and after (right) its exposure to molecular hydrogen at 1 bar at 50 °C for 3 d. White curves show the profiles along the membrane's diameter. No changes in membrane positions could be detected within our experimental accuracy. **b**, Same experiment for monolayer MoS$_2$. No changes could be noticed either. **c**, For comparison, we show the simultaneous experiment for a microcontainer covered with monolayer graphene. The membrane clearly bulged out after the exposure, similar to the case of Fig. 2a. All scale bars, 1 μm. After the experiment, the bulging membrane in **c** was kept under ambient conditions and found to slowly deflate over months, in agreement with the room-temperature permeation rates reported in the main text.
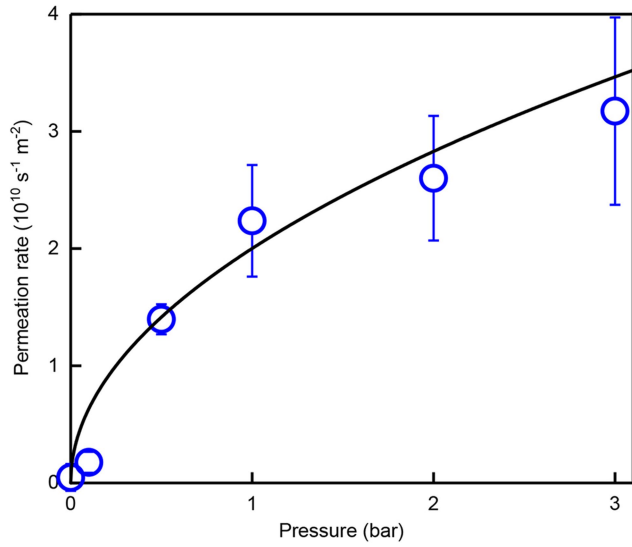
Extended Data Fig. 5 | Pressure dependence of hydrogen permeation.
Symbols are measurements at room temperature. Error bars are standard
deviation using a minimum of ten devices in each case. Solid curve is the best fit
to the square-root dependence.
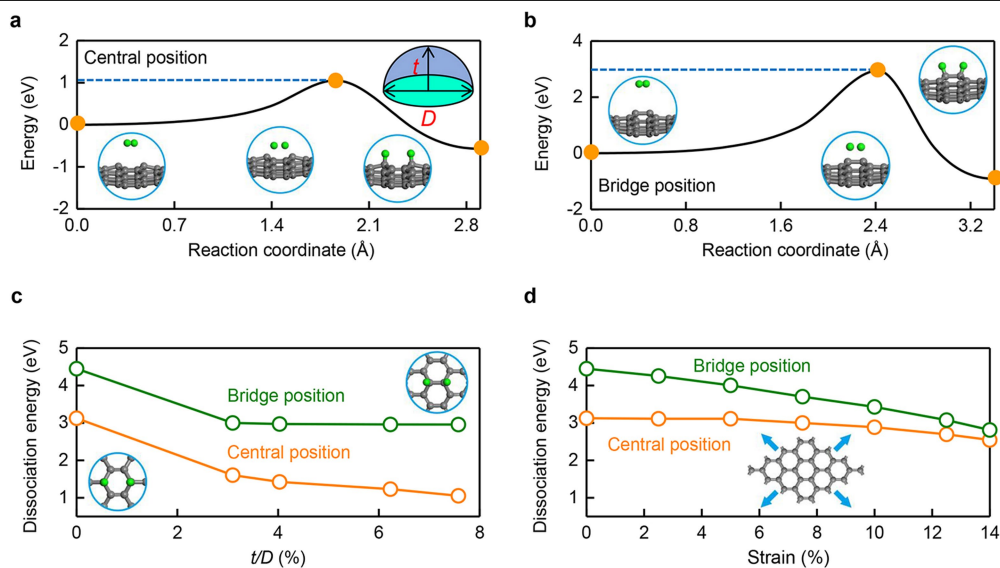
Extended Data Fig. 6 | Dissociation of molecular hydrogen at graphene ripples. a, **b**, Reaction of molecular hydrogen with graphene for $t/D = 7.5\%$ if adatoms are adsorbed in the central (**a**) and bridge (**b**) positions. Insets: atomic configurations of the initial, maximum-energy and final states (marked by the orange dots). The simulated size D is 2–3 nm. **c**, The dissociation barrier as a function of ripples' curvature. Insets show top view of the bridge and central positions for hydrogen adatoms. **d**, The dissociation energy barrier as a function of biaxial strain. The inset shows schematic showing the direction of applied strain in our simulations.

a

b

c
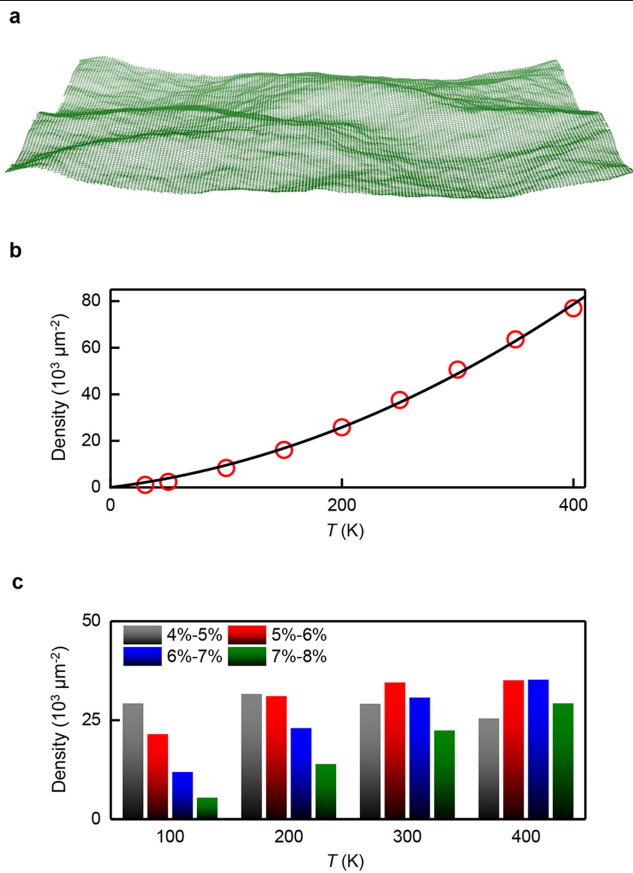
Extended Data Fig. 7 | Intrinsic (dynamic) ripples in graphene at different temperatures. a, Typical snapshot of graphene membrane at 300 K using molecular dynamics simulations. **b**, Density of ripples with $t/D \geq 7\%$ (most chemically active). Symbols are the calculations for different T. Solid curve is a guide to the eye. **c**, Statistical distribution of intrinsic ripples with different t/D.
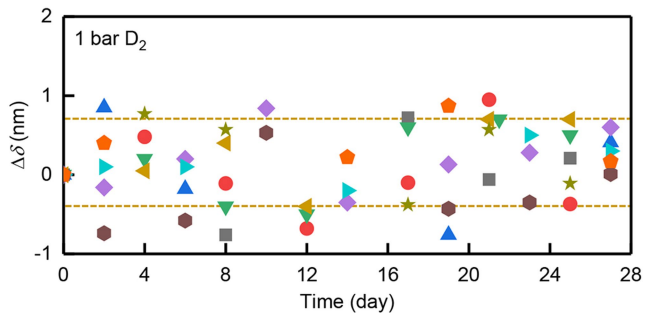
Extended Data Fig. 8 | Isotope effect. Time evolution of $\Delta\delta$ for ten different devices (different colours) exposed to deuterium at 1 bar at room temperature (295 ± 2 K). All the devices are hBN containers sealed with monolayer graphene. The dashed lines indicate maximum changes detected for the device coded with the same colour. The random fluctuations are close in amplitude to those shown in Fig. 1e for helium.